

PULSE PROFILES FROM SPINNING NEUTRON STARS IN THE HARTLE-THORNE APPROXIMATION

DIMITRIOS PSALTIS¹ AND FERYAL ÖZEL^{1,2}

Astronomy Department, University of Arizona, 933 N. Cherry Ave., Tucson, AZ 85721, USA
Draft version May 6, 2019

ABSTRACT

We present a new numerical algorithm for the calculation of pulse profiles from spinning neutron stars in the Hartle-Thorne approximation. Our approach allows us to formally take into account the effects of Doppler shifts and aberration, of frame dragging, as well as of the oblateness of the stellar surface and of its quadrupole moment. We confirm an earlier result that neglecting the oblateness of the neutron-star surface leads to $\simeq 5 - 30\%$ errors in the calculated profiles and further show that neglecting the quadrupole moment of its spacetime leads to $\simeq 1 - 5\%$ errors at a spin frequency of $\simeq 600$ Hz. We discuss the implications of our results for the measurements of neutron-star masses and radii with upcoming X-ray missions, such as NASA's NICER and ESA's LOFT.

Subject headings: stars: neutron — relativity — gravitation

1. INTRODUCTION

A temperature anisotropy on the surface of a spinning neutron star leads to a periodic oscillation of its brightness at the stellar spin frequency, as viewed by an observer at infinity. The amplitude and spectrum of this oscillation depends on the temperature profile on the stellar surface, on the beaming of the emerging radiation, and on the magnitude of strong-field gravitational lensing experienced by the photons as they propagate through the neutron-star spacetime (Pechenick, Ftaclas, & Cohen 1983). Given a model for the emerging radiation, the properties of the brightness oscillation can, therefore, be used in mapping the neutron-star surface and spacetime, as well as in measuring its mass and radius.

Pulse-profile modeling techniques have been used to explore the surface emission properties in many types of neutron stars, such as slow pulsars (Page 1995), magnetars (DeDeo, Psaltis, & Narayan 2001; Özel, Psaltis, & Kaspi 2001), rotation-powered millisecond pulsars (Pavlov & Zavlin 1997; Bogdanov, Rybicki, & Grindlay 2007), X-ray bursters (Weinberg, Miller, & Lamb 2001; Nath, Strohmayer, & Swank 2002; Muno, Özel, & Chakrabarty 2002, 2003), and accretion-powered millisecond pulsars (Poutanen & Gierlinski 2003; Bhat-tacharyya et al. 2005; Leahy et al. 2008, 2009, 2001; Lamb et al. 2009; Morsink & Leahy 2011). This technique also defines the key scientific objectives of several upcoming or proposed X-ray missions, such as NASA's NICER (Arzoumanian et al. 2010), ESA's LOFT (Ferrocio et al. 2012), and ISRO's Astrosat (Agrawal 2006), which aim to measure the masses and radii of several millisecond rotation-powered pulsars and X-ray bursters with high precision.

The effects of the gravitational lensing on the surface photons have been explored with a variety of techniques

and approximations, since the original work on non spinning neutron stars (Pechenick, Ftaclas, & Cohen 1983). At relatively low spin frequencies (i.e., $\lesssim 300$ Hz), the spacetime of the neutron star is accurately described by the Schwarzschild metric and its spin primarily causes Doppler shifts and aberration (Miller & Lamb 1998; Muno, Özel, & Chakrabarty 2002; Poutanen & Beloborodov 2006). At similar spin frequencies, the effects of frame dragging are marginal (Braje, Romani, & Rauch 2000). At moderate spin frequencies (i.e., $\lesssim 800$ Hz), the neutron-star spacetime acquires a quadrupole moment and its surface becomes oblate. Finally, at spin frequencies near breakup (i.e., $\gtrsim 1$ kHz), higher order multipoles become important and the neutron-star spacetimes can only be calculated by solving numerically the field equations for particular equations of state (Cook et al. 1994; Stergioulas & Friedman 1995; Stergioulas 2003; see also Cadeau et al. 2007).

Rotation powered millisecond pulsars and thermonuclear X-ray bursters, which make up the majority of neutron star targets for NICER and LOFT, have fast spin frequencies in the $\simeq 300 - 800$ Hz range. Stars with these spin frequencies, especially if they also possess larger radii, acquire notably oblate shapes and large quadrupole moments. Morsink et al. (2007) demonstrated that, for this relevant range of parameters, the oblateness of the neutron-star surface significantly affects the resulting pulse profiles. In a similar range of frequencies, Bauböck, Psaltis, & Özel (2013) showed that the quadrupole moment of a neutron-star spacetime also significantly alters the spectroscopic properties of its surface emission.

In the present article, we describe a new algorithm for calculating the lightcurves of spinning neutron stars in the Hartle-Thorne approximation, which formally takes into account the oblateness and quadrupole moment of the star, as well as the effects of frame dragging, Doppler shift, and aberration. Contrary to calculations that are based on numerical spacetimes, our approach allows us to simulate lightcurves based only on the macroscopic properties of the neutron stars, without the need for assuming a particular equation of state.

dpsaltis, fozel@email.arizona.edu

¹also, Institute for Theory and Computation, Harvard-Smithsonian Center for Astrophysics, 60 Garden St., Cambridge, MA 02138

²also, Radcliffe Institute for Advanced Study, Harvard University, 8 Garden St., Cambridge, MA 02138

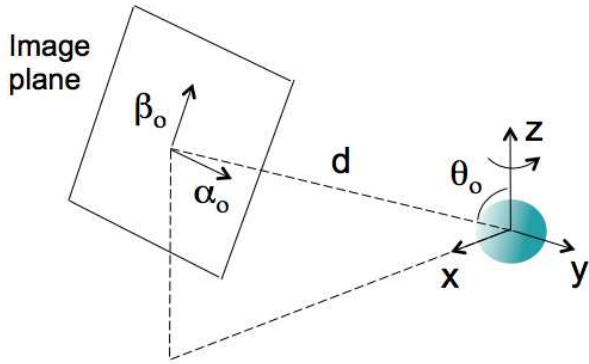


FIG. 1.— The geometry used in calculating the lightcurves from spinning neutron stars.

In §2, we describe our calculations that are based on our ray-tracing algorithm described in Psaltis & Johannsen (2012) and Bauböck et al. (2012). In §3, we compare our calculations with earlier results obtained under different assumptions and approximations. Finally, in §4, we discuss the implications of our results for the mass and radius measurements with the upcoming X-ray missions.

2. CALCULATING LIGHTCURVES OF SPINNING NEUTRON STAR

Our goal is to calculate the brightness and the spectrum of emission from the surface of a spinning neutron star at different rotational phases and for different viewing geometries. To this end, we define a coordinate system with its origin at the center of the neutron star and the z -axis aligned with the rotation axis of the star. We then set up an image (or detector) plane at a distance d from the center and at an angle θ_0 with respect to the rotational axis of the star. At $\theta_0 = 0$, the image plane is parallel to the $x-y$ plane, while for $\theta_0 = \pi/2$, the vector d lies along the x -axis and the image plane is parallel to the $y-z$ plane. On the image plane, we also define a two-dimensional Cartesian coordinate system (α_0, β_0) , with the β_0 -axis on the $x-z$ plane and the α_0 -axis pointing towards the y -axis (see Figure 1).

The flux of radiation at photon energy E received on the image plane at time t is given by the integral

$$F_E(t) = \frac{1}{d^2} \int_{\alpha_0, \beta_0} I(\alpha_0, \beta_0; E, t) d\alpha_0 d\beta_0, \quad (1)$$

where $I(\alpha_0, \beta_0; E, t)$ is the specific intensity on the image plane of a point with coordinates (α_0, β_0) . Of all the photon rays that reach the image plane, only those that originate on the neutron-star surface have a non-zero intensity. Because of the strong gravitational field of the neutron star, these photon rays are not straight but are rather curved due to gravitational lensing.

The radii of all realistic neutron stars are larger than the radius of the photon orbit in their spacetimes. Under these conditions, photons arriving at position (α_0, β_0) on the image plane are uniquely connected to a position and direction on the stellar surface. As a result, we can define a number of one-to-one maps between the coordinates

(α_0, β_0) at which a photon ray crosses the image plane and various other properties of the photons that travel along this ray. In particular, we will use the five maps

$$\phi = \phi(\alpha_0, \beta_0) \quad (2)$$

$$\theta = \theta(\alpha_0, \beta_0) \quad (3)$$

$$\delta = \delta(\alpha_0, \beta_0) \quad (4)$$

$$\epsilon = \frac{E(\alpha_0, \beta_0)}{E_e(\phi, \theta)} \quad (5)$$

$$t_d = t_d(\alpha_0, \beta_0), \quad (6)$$

that connect the image-plane coordinates (α_0, β_0) of a photon ray to the longitude ϕ and latitude θ on the neutron star surface where the ray originates, to the angle δ between the photon momentum on the stellar surface and the normal to the surface, to the ratio ϵ between the observed and emitted energies, E and E_e , and to the time of flight between the neutron star surface and the image plane.

Because of the Lorentz invariance of the photon occupation number along a photon ray, we can now relate the specific intensity $I(\alpha_0, \beta_0; E, t)$ on the image plane to the specific intensity $I_{\text{NS}}(\theta, \phi, \delta; E, t)$ on the neutron star surface as

$$I(\alpha_0, \beta_0; E, t) = \epsilon^3 I_{\text{NS}} \left[\phi(\alpha_0, \beta_0), \theta(\alpha_0, \beta_0), \delta(\alpha_0, \beta_0); \frac{E}{\epsilon}, t - t_d(\alpha_0, \beta_0) \right]. \quad (7)$$

Inserting this last expression into equation (1) leads to an integral expression for the time- and energy-dependent radiation flux that flows through the image plane.

2.1. Ray Tracing

We calculate the five mapping relations (2)-(6) using the ray tracing algorithm described in Psaltis & Johannsen (2012) and Bauböck et al. (2012). In this algorithm, we describe the external spacetime of a neutron star spinning at a moderate rate using the variant of the Hartle-Thorne metric developed by Glampedakis & Babak (2006).

The metric coefficients depend on the mass M of the neutron star, on its specific angular momentum a , and on the mass quadrupole moment q of the spacetime. We choose to write the quadrupole moment as

$$q = -a^2(1 + \eta), \quad (8)$$

for two reasons. First, when $\eta = 0$, the quadrupole moment of the spacetime reduces to that of the Kerr metric. Second, calculations of the quadrupole moments of spinning neutron stars using numerical algorithms (Laarakkers & Poisson 1998; Pappas & Apostolatos 2012) showed that equation (8) remains valid even for neutron stars that are spinning near their breakup points. Typical values of the quadrupole moment require $\eta \sim 1 - 6$, depending on the equation of state, as well as on the stellar mass and radius.

The shape of a neutron star spinning at moderate rates deviates from spherical. In the Hartle-Thorne approximation, the dependence of the neutron-star radius on the polar angle θ can be written in terms of two parameters, which we choose to be the equatorial and the polar radius

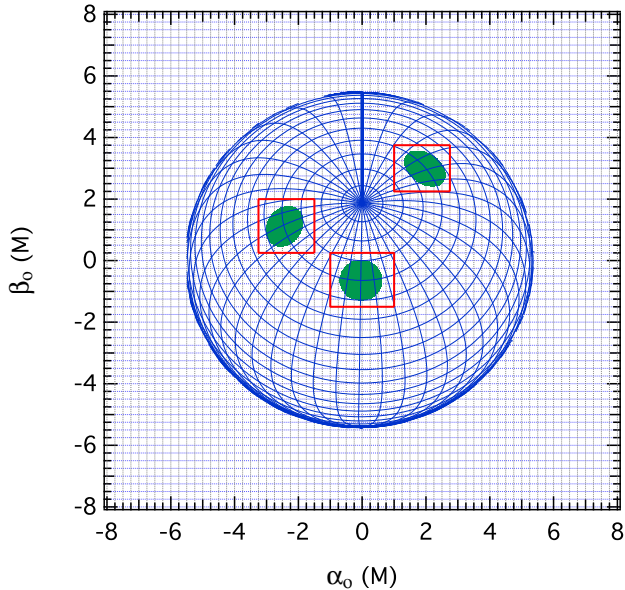


FIG. 2.— An illustration of the two grids used in a typical calculation of a lightcurve from a spinning neutron star. The image plane has a size of $16GM/c^2$ on which we have set up a 65×65 grid. Contours of constant latitude and longitude are shown in 10° intervals on the neutron star surface. A 10° hot spot on the neutron star is shown at a colatitude of 40° and at three different rotational phases: $\omega t = 0, \pi/2$, and $2\pi/3$. The red rectangles outline the regions in the low-resolution grid within which we set up a 256×256 high-resolution grid, for each rotational phase. In this figure, the inclination of the observer is 30° , the neutron star has a mass of $1.8 M_\odot$, a radius of 10 km, other parameters that are typical of the FPS equation of state, and is spinning at 600 Hz in the clockwise direction.

of the star, R_p and R_{eq} , as

$$\frac{R(\theta)}{R_{\text{eq}}} = \sin^2 \theta + \frac{R_p}{R_{\text{eq}}} \cos^2 \theta. \quad (9)$$

For the purposes of the calculations reported in this paper, we use the analytic fitting formula for the ratio of the polar to the equatorial radius devised by Morsink et al. (2007) as discussed in Bauböck et al. (2012). Moreover, the equatorial radii that we are reporting are defined such that the proper circumference of a circle in the equator at radius R_{eq} is equal to $2\pi R_{\text{eq}}$. In all the simulations presented hereafter, the value of the neutron star radius quoted represents R_{eq} at the specified spin frequency.

Finally, we need to specify the intensity of radiation on the stellar surface. In this paper, we will assume that radiation emerges only from a small circular spot of angular radius ρ that is fixed at a colatitude θ_s with respect to the rotational pole of the neutron star. The spectrum of the emerging radiation is that of a blackbody of temperature T_{NS} and the emission is isotropic. Because we will be reporting our results with the photon energy expressed in units of T_{NS} , the latter quantity will not represent an additional parameter in our calculations.

In summary, the lightcurve from a spinning neutron star in the Hartle-Thorne approximation and with the approximations discussed above depends on the following parameters: (i) the mass M of the neutron star; (ii) the equatorial radius R_{eq} of the neutron star; (iii) its specific angular momentum a ; (iv) the quadrupole moment of its spacetime as measured by the parameter η ; (v) the

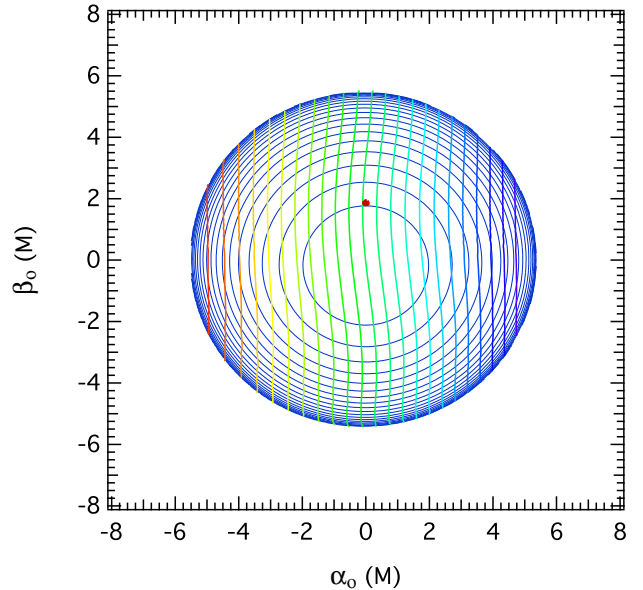


FIG. 3.— Contours of constant (blue curves) time delay and (rainbow curves) ratio of observed to emitted photon energy from the neutron star shown in Figure 2. The time-delay contours are at equidistant intervals in the range $(0.5 - 10) \times GM/c^2$; the photon-energy contours are at equidistant intervals in the range 0.62–0.74. The red dot marks the location of the north rotational pole of the neutron star.

observer inclination θ_0 ; (vi) the colatitude of the spot θ_s ; and (vii) the angular radius of the spot ρ .

2.2. Discretization, Convergence, and Performance

In order to calculate efficiently the flux of radiation through the image plane, especially when the size of the emitting region is very small, we evaluate the integral (1) using a set of two nested grids, as shown in Figure 2. We initially use the ray-tracing algorithm to calculate and store the five mapping relations (2)-(3) on a low-resolution grid of $N_l \times N_l$ points, with a typical value of $N_l = 65$. For each rotational phase of the neutron star, we use these results in order to outline a rectangular region in the low-resolution grid that surrounds the projection of the emitting region on the image plane (shown as red rectangles in Figure 2 for three rotational phases). We then set up a high-resolution grid within each of these rectangular regions of $N_h \times N_h$ points, with a typical value of $N_l = 256$. Finally, we use the ray-tracing algorithm to calculate the mapping relations on the high-resolution grid and evaluate numerically the integral (1) only within this grid using a trapezoid integration.

Attaining a sufficiently high resolution for the first three of the five mapping relations (2)-(6) is what drives the requirement for a high-resolution grid. This is shown in Figure 2, where contours of constant latitude and longitude on the neutron star surface (in intervals of 10° , which is the same magnitude as the angular size of the spot in this example) are projected on the image plane. The separation of nearby contours decreases rapidly from the center of the stellar image to its edge; therefore, the number of image plane points falling within a spot near the edges also declines rapidly. The outline of even a large spot of an angular radius of 10° , as in this example, would be barely resolvable in the low-resolution grid shown in the figure as the spot makes its way to-

wards the edge of the stellar image. In contrast, the last two mapping relations (5)-(6) can be well approximated even on the low-resolution grid. This is shown in Figure 3, in which contours of constant energy ratios ϵ and time delays t_d are plotted on the image plane. As expected, the contours of constant redshift are nearly vertical curves spanning a narrow range, whereas the contours of constant time delay are nearly concentric circles, centered at the origin of the α_0, β_0 plane. In more detail, the waviness of the redshift contours arises from two competing effects: the frame-dragging correction to the magnitude of the surface velocity as measured by a zero-angular-momentum observer and the quadrupole correction to the gravitational redshift. Note that the redshift contours are further distorted and develop the island and saddle shapes shown, e.g., in the right panel of Figure 5 of Bauböck et al. (2013), when the neutron star is viewed from a smaller inclination angle and has a larger quadrupole moment. The frame-dragging and the quadrupole corrections to the time-delay contours are typically less than 1/1000 of the neutron star spin period and are, therefore, negligible.

The convergence of the ray-tracing algorithm was demonstrated in Psaltis & Johannsen (2012), where the results were also compared to other algorithms for calculating the profiles of relativistically broadened fluorescent lines around black holes. In Figure 4, we derive numerically the convergence rate of our integration algorithm for the calculation of the radiation flux. We have taken the calculation shown in Figure 2, with a high-resolution grid of 512×512 points nested in a low resolution grid of 65×65 points as the fiducial one and calculated the time-dependent flux at a photon energy of $E = 3k_B T_{\text{NS}}$ at 32 phase bins. We then repeated the same calculation with $N_h = 16, 32, 64, 128,$ and 256 grid points along each dimension of the high-resolution grid and compared these lower-resolution runs with the fiducial calculation. We plot in Figure 4 the r.m.s. fractional difference between each of the lower-resolution runs and the fiducial run, as a function of the number of grid points used. The blue line shows the best-fit power-law relation between the two quantities plotted, with the fractional difference scaling approximately as $\sim N_h^{-1.56}$. This convergence rate is determined predominantly by the ability of the two-dimensional grid to trace the shape of the deformed circular spot, as the latter is projected onto the image plane.

Figure 4 demonstrates that a high-resolution grid of 128×128 points leads to an accuracy of one part in thousand, which is adequate for most applications. A typical calculation takes approximately one second per phase bin on a fast workstation. This time can be reduced by up to two orders of magnitude if the ray-tracing part of the algorithm is performed on a GPU card (see Chan, Psaltis, & Özel 2013).

2.3. Comparison with Earlier Calculations

Figure 5 compares three lightcurves for a slowly spinning (1 Hz) neutron star calculated with the current algorithm to the results presented by Pechenick et al. (1983) in their Figure 10. For this particular comparison, the beaming of the emission that emerges from the stellar surface was taken to be proportional to $\sin \delta$. The

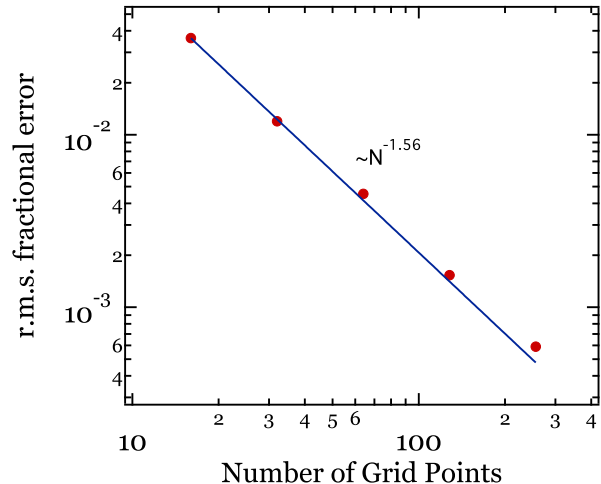


FIG. 4.— Convergence plot for the configuration shown in Figure 2. Calculations with different numbers of points in the high-resolution grid are compared to a fiducial calculation that has 512×512 grid points. The rms fractional error between their lightcurves in 32 phase bins is shown as a function of the number of grid points. The solid line shows the best fit slope of $\sim N^{-1.56}$, which is determined mainly by the ability of the 2D rectangular grid to trace the shape of the deformed circular spot.

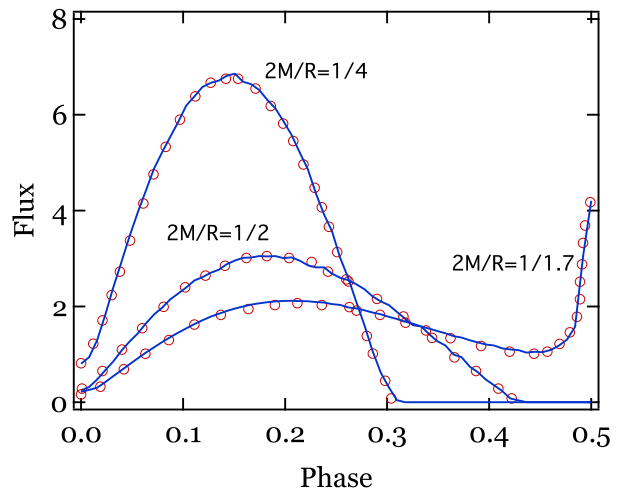


FIG. 5.— The flux of radiation from slowly-spinning neutron stars with different values of the compactness $2GM/Rc^2$, emitting from a single hot spot, as a function of the spin phase. The open circles are taken from Figure 10 of Pechenick et al. (1983), while the solid curves are the profiles calculated in the present work. The inclination of the observer is 90° , the hot spot is on the stellar equator, its angular half-size is 5° , and the radiation emerges from its surface with a beaming proportional to $\sin \delta$.

three different lightcurves correspond to neutron stars with increasing compactness, from $2GM/Rc^2 = 1/4$ to $2GM/Rc^2 = 1/1.7$. As expected, at this low spin frequency, the Doppler effects, as well as those of frame dragging, oblateness, and of the spacetime quadrupole moment are negligible.

Figure 6 compares two additional lightcurves with the results shown in Figure 2 of Poutanen & Beloborodov (2003), who used the Schwarzschild+Doppler approximation. Because we consider this to be a verification comparison, we artificially set the frame dragging, the stellar oblateness, and the spacetime quadrupole to zero

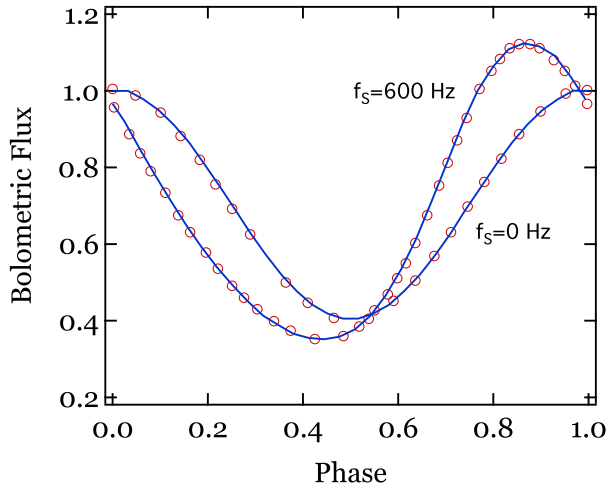


FIG. 6.— The bolometric flux of radiation from neutron stars with different spin frequencies, emitting from a single hot spot, in the Schwarzschild+Doppler approximation. The open circles are taken from Figure 2 of Poutanen & Beloborodov (2003), while the solid curves are the profiles calculated in the present work. The inclination of the observer is 45° , the colatitude of the hot spot is 45° , its angular half-size is 5° , and the radiation emerges from its surface with isotropic beaming. The neutron stars have a mass of $1.4 M_\odot$ and a compactness of $2GM/Rc^2 = 1/2.5$.

in our calculations. As discussed in, e.g., Braje et al. (2000) and Poutanen & Beloborodov (2003), Doppler shifts and aberration have three main effects on the pulse profiles: they increase their amplitudes, they shift the location of their maxima to earlier phases, and they introduce an asymmetry to the profile. Even though in our approach the effects of Doppler shifts and of aberration are calculated automatically and cannot be separated from those of the gravitational lensing and of the gravitational redshift, our results agree, as expected, with the earlier approximate methods.

3. RESULTS

We now explore the effects of the stellar oblateness and of the spacetime quadrupole moment on the pulse profiles. Figure 7 shows the result of incorporating these two effects, one at a time, on the pulse profile calculated for a $1.8 M_\odot$, 15 km neutron star described by the equation of state L and spinning at 600 Hz (see Bauböck et al. 2012 for a description of the equations of state and their relevant parameters). This rather large radius for the neutron star, albeit disfavored by current observations (see Özel 2013 and references therein), leads to the largest Doppler, oblateness, and quadrupole effects. The left panel of the figure shows the pulse profiles at three different observer inclinations at a photon energy equal to three times the surface temperature, which roughly corresponds to the peak of the spectrum (before applying the gravitational and Doppler shifts). The right panel shows the pulse profile at a single observer inclination but for three different photon energies.

As discussed in Morsink et al. (2007), taking into account the oblateness of the stellar surface significantly reduces the amplitude of pulsations. Comparing the pulse profiles of two neutron stars with the same equatorial radius but different surface shapes, an increasing oblateness both increases the gravitational redshift experienced by

photons leaving a non-equatorial emitting region as well as alters the relative orientation of the emitting region with respect to the distant observer. The net effect is a decrease in the observed flux at the peak of the pulse profile. Moreover, the oblate shape of the stellar surface alters the visibility of different regions of the surface by a distant observer and changes the flux at the minimum of the pulse profile. The phase of the maximum flux and the asymmetry of the profile, both of which are predominantly determined by Doppler effects are not altered significantly. Taking into account the oblateness of the stellar surface while still neglecting the quadrupole of the spacetime corrects for most of the difference between the Schwarzschild+Doppler and the Hartle-Thorne approximations.

The quadrupole of the spacetime alters the pulse profiles primarily through its effects on the gravitational redshift experienced by photons. As discussed in Bauböck et al. (2013), the spacetime quadrupole competes with the Doppler shifts in determining the energy and brightness of the emerging radiation. As the observer inclination is reduced, the Doppler effects become less important and the redshift experienced by the photons is dominated by the spacetime quadrupole.

Figures 8 and 9 show that the pulse profiles for the same set up and observer inclinations, but for a neutron star spinning at 300 Hz and for a 10 km neutron star, respectively. These figures show that, as expected, the effects of the stellar oblateness and of the spacetime quadrupole become less important as the spin frequency of the neutron star or its equatorial radius are reduced. The correction introduced by the oblateness of the neutron star, albeit small, still dominates the correction introduced by the spacetime quadrupole.

Figure 10 quantifies the magnitudes of the errors introduced in the calculation of the pulse profiles by neglecting the stellar oblateness and the spacetime quadrupole. As expected from the above discussion, the effects of the stellar oblateness become large as the observer inclination becomes very different from the colatitude of the emitting region but have a weak dependence on photon energy. On the other hand, the effects of the spacetime quadrupole have a stronger energy dependence and become more significant (in absolute value) as the inclination of the observer is reduced. This is consistent with the fact that quadrupole effects arise primarily from the influence of the spacetime quadrupole on the gravitational redshift experienced by the photons and their relative contribution to the observed flux increases as the Doppler effects become less pronounced.

The overall effects of the stellar oblateness and of the spacetime quadrupole for a 600 Hz spin frequency are of order $\sim 10 - 30\%$ and $\sim 1 - 5\%$, respectively, depending on the radius of the neutron star and the observer inclination. These are comparable to the stated 5% target uncertainty in the measurement of neutron-star masses and radii using observations of pulse profiles with NICER and LOFT. As a consequence, achieving the goals of these two missions requires calculating pulse profiles with both these effects taken into account.

We thank Michi Bauböck for many useful discussions on ray tracing in neutron-star spacetimes and the referee

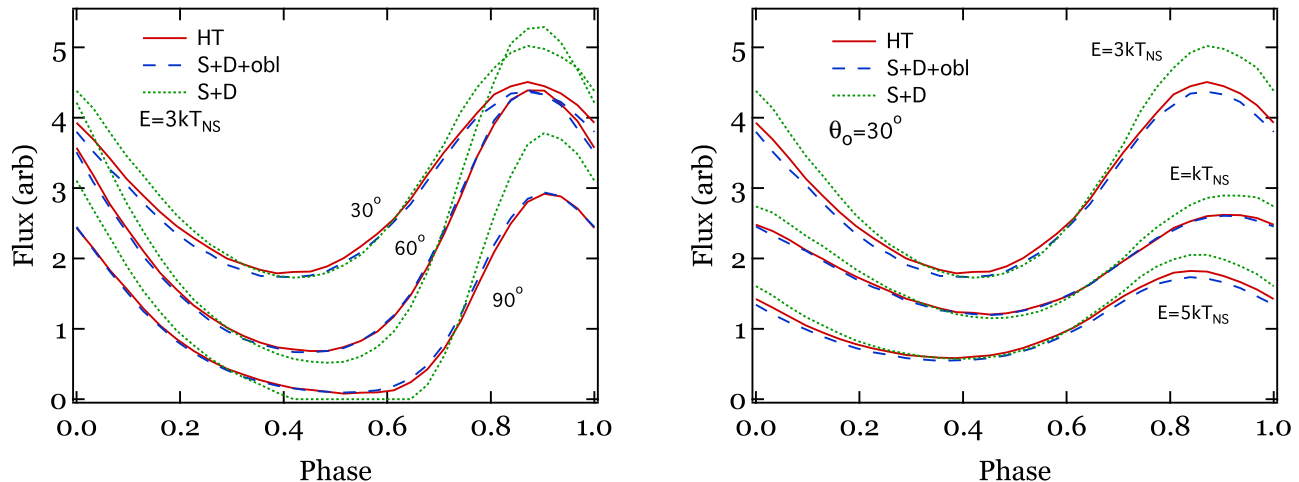


FIG. 7.— The flux of radiation received from a spinning neutron star (*Left*) for a photon energy equal to three times the neutron-star temperature but observed at different inclinations and (*Right*) at an observer inclination of 30° but for three different photon energies. In both panels, the solid red line shows the calculation with the Hartle-Thorne metric, the dashed blue line shows the calculation in the Schwarzschild+Doppler approximation with the oblateness of the neutron star taken into account, and the dotted green line shows the calculation in the Schwarzschild+Doppler approximation. All calculations correspond to a $1.8 M_\odot$ neutron star, with an equatorial radius R_{eq} fixed to 15 km, spinning at 600 Hz, and with values for the remaining parameters that are typical for the L equation of state. The emitting region is taken to be a circular hot spot with a semi-angular size of 10° and positioned at a colatitude of 40° from the stellar rotational pole. The emission is that of a blackbody, with isotropic beaming. All fluxes have been multiplied by the same, constant factor for clarity.

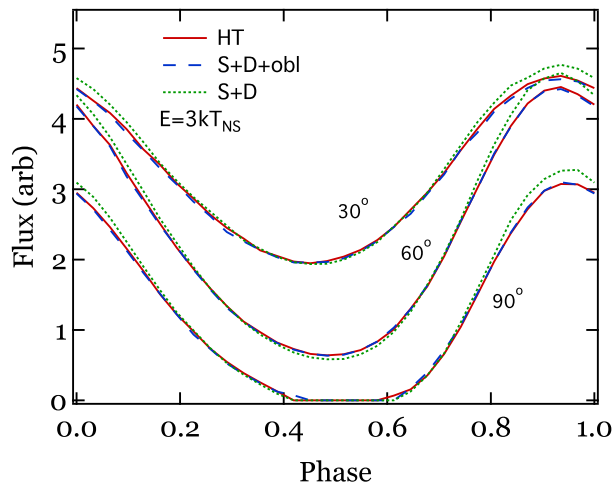


FIG. 8.— Same as in the left panel of Figure 7 but for a neutron star spinning at 300 Hz.

Sharon Morsink for enlightening discussions and comments. This work was supported in part by NSF grant AST-1108753, NSF CAREER award AST-0746549, and Chandra Theory grant TM2-13002X. F.Ö. gratefully acknowledges support from the Radcliffe Institute for Advanced Study at Harvard University.

REFERENCES

- Agrawal, P. C. 2006, *Advances in Space Research*, 38, 2989
 Bauböck, M., Psaltis, D., Özel, F. 2013, *ApJ*, 766, 87
 Bauböck, M., Psaltis, D., Özel, F., & Johannsen, T. 2012, *ApJ*, 753, 175
 Bhattacharyya, S., Strohmayer, T. E., Miller, M. C., & Markwardt, C. B. 2005, *ApJ*, 619, 483
 Bogdanov, S., Rybicki, G. B., & Grindlay, J. E. 2007, *ApJ*, 670, 668
 Braje, T. M., Romani, R. W., & Rauch, K. P. 2000, *ApJ*, 531, 447
 Cadeau, C., Morsink, S. M., Leahy, D., & Campbell, S. S. 2007, *ApJ*, 654, 458
 Chan, C.-K., Psaltis, D., & Özel, F. 2013, *ApJ*, submitted
 Cook, G. B., Shapiro, S. L., & Teukolsky, S. A. 1994, *ApJ*, 424, 823
 DeDeo, S., Psaltis, D., & Narayan, R. 2001, *ApJ*, 559, 346
 Glampedakis, K., & Babak, S. 2006, *Classical and Quantum Gravity*, 23, 4167
 Hartle, J. B., & Thorne, K. S. 1968, *ApJ*, 153, 807
 Laarakkers, W. G., & Poisson, E. 1999, *ApJ*, 512, 282
 Lamb, F. K., Boutloukos, S., Van Wassenhove, S., et al. 2009, *ApJ*, 706, 417
 Leahy, D. A., Morsink, S. M., & Cadeau, C. 2008, *ApJ*, 672, 1119
 Leahy, D. A., Morsink, S. M., & Chou, Y. 2011, *ApJ*, 742, 17
 Leahy, D. A., Morsink, S. M., Chung, Y.-Y., & Chou, Y. 2009, *ApJ*, 691, 1235
 Miller, M. C., & Lamb, F. K. 1998, *ApJ*, 499, L37
 Morsink, S. M., Leahy, D. A., Cadeau, C., & Braga, J. 2007, *ApJ*, 663, 1244
 Morsink, S. M., & Leahy, D. A. 2011, *ApJ*, 726, 56
 Muno, M. P., Özel, F., & Chakrabarty, D. 2002, *ApJ*, 581, 550
 ———. 2003, *ApJ*, 595, 1066
 Nath, N. R., Strohmayer, T. E., & Swank, J. H. 2002, *ApJ*, 564, 353
 Özel, F. 2013, *Reports on Progress in Physics*, 76, 016901
 Özel, F., Psaltis, D., & Kaspi, V. M. 2001, *ApJ*, 563, 255
 Page, D. 1995, *ApJ*, 442, 273

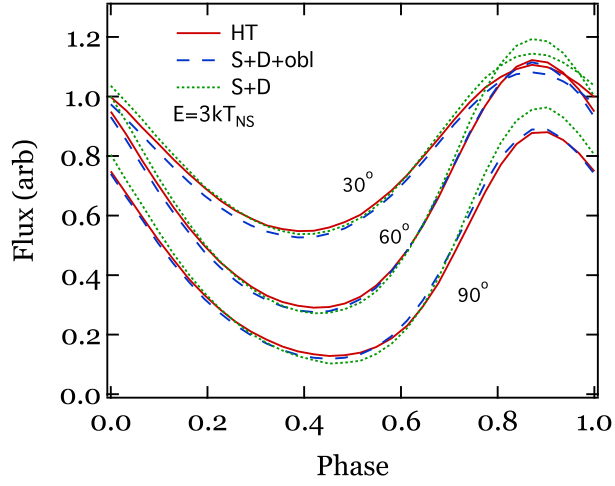


FIG. 9.— Same as in the left panel of Figure 7 but for a $1.8 M_{\odot}$, 10 km neutron star, spinning at 600 Hz, with parameters that are typical for the FPS equation of state.

- Pappas, G., & Apostolatos, T. A. 2012, *Physical Review Letters*, 108, 231104
Pechenick, K. R., Ftaclos, C., & Cohen, J. M. 1983, *ApJ*, 274, 846
Psaltis, D., & Johannsen, T. 2012, *ApJ*, 745, 1
Poutanen, J., & Gierliński, M. 2003, *MNRAS*, 343, 1301
Poutanen, J., & Beloborodov, A. M. 2006, *MNRAS*, 373, 836
Stergioulas, N. 2003, *Living Reviews in Relativity*, 6, 3
Stergioulas, N., & Friedman, J. L. 1995, *ApJ*, 444, 306
Weinberg, N., Miller, M. C., & Lamb, D. Q. 2001, *ApJ*, 546, 1098

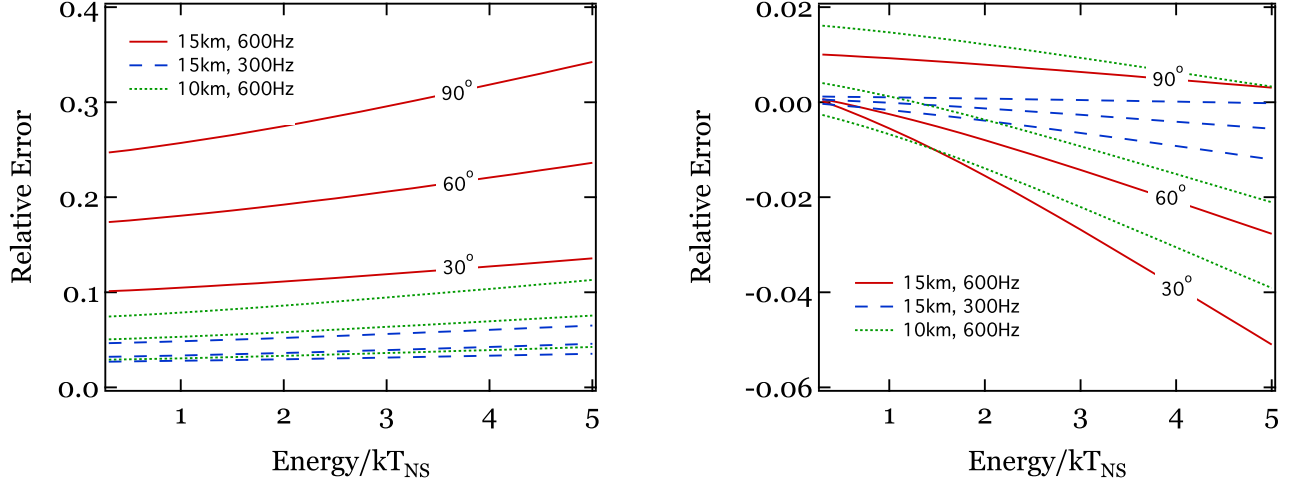


FIG. 10.— The energy dependence of the relative errors of the flux at spin phase 0.9 with the respect to the calculation in the Hartle-Thorne metric of (*Left*) the Schwarzschild+Doppler approximation with spherical neutron stars and (*Right*) of the Schwarzschild+Doppler approximation with the oblateness of the neutron stars taken into account. The various line styles correspond to the different calculations shown in Figures 7-9: the solid red curves are for the 15 km neutron stars spinning at 600 Hz shown in Figure 7; the dashed blue curves are for the 15 km neutron star spinning at 300 Hz shown in Figure 8; the dotted green curves for the 10 km neutron star spinning at 600 Hz shown in Figure 9. In each case, the three curves of the same style correspond, from top to bottom, to observer inclinations of 90°, 60°, and 30°, respectively.